Sustainable Energy, Grids and Networks 46 (2026) 102263

Contents lists available at ScienceDirect

Sustainable Energy, Grids and Networks

journal homepage: www.elsevier.com/locate/segan

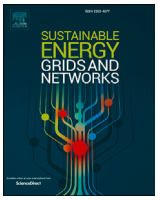

Dynamic thermal rating of offshore cables: An electro-thermal and economic framework for enhanced renewable integration

Mojtaba Moradi-Sepahvand*, Farzad Nasirpour

Department of Wind Energy, Energy and Materials Transition Unit, TNO, Rijswijk, South Holland, the Netherlands

ARTICLE INFO

Keywords:
Dynamic thermal rating
Electro–thermal modeling
Optimal power flow
Offshore wind farms
Submarine HVAC cables

ABSTRACT

Dynamic Thermal Rating (DTR) enables real-time adjustment of HVAC submarine export cable capacity based on prevailing operating and environmental conditions, which offers a practical means to enhance offshore wind farm (OWF) export capability. This paper presents an integrated electro-thermal and Optimal Power Flow (OPF) framework, formulated as a binary-free Linear Programming (LP) problem, to co-optimize OWF generation dispatch and cable loading under DTR. The electro-thermal model, validated against high-fidelity finite element method (FEM) in COMSOL Multiphysics, accurately captures steady-state and transient heat transfer within the cable and surrounding seabed. Application to realistic offshore wind farm configurations, including overplanting and hybrid solar–wind scenarios, demonstrates that applying DTR to HVAC export cables can substantially reduce renewable energy curtailment, improve utilization of existing infrastructure, and defer the need for costly reinforcements. The results highlight DTR as a technically robust and economically attractive strategy to increase renewable energy delivery and support higher integration levels in offshore transmission systems.

1. Introduction

The deployment of offshore wind farms (OWFs) is accelerating globally, driven by ambitious renewable energy targets and the urgent need to decarbonize the electricity sector. In Europe, installed offshore wind capacity has grown substantially over the past decade, supported by advances in turbine technology, economies of scale, and favorable policy frameworks [1]. OWFs are increasingly being developed farther from shore and in deeper waters to access higher and more stable wind resources, with individual projects now reaching capacities on the gigawatt scale. Achieving the European Commission's target of 230–450 GW of offshore wind by 2050 [2] will require not only continued investment in generation assets but also significant innovation in transmission systems to deliver power efficiently and reliably to onshore grids.

Export systems, typically based on high-voltage alternating current (HVAC) or high-voltage direct current (HVDC) technologies, represent critical infrastructure and one of the largest capital expenditures in OWFs [3]. HVAC submarine cables, in particular, are widely used for short to medium transmission distances due to their maturity and cost-effectiveness. However, their thermal limits often constrain export capacity, leading to renewable energy curtailment, reduced asset utilization, and higher Levelized Cost of Energy (LCOE). Traditionally, cable ampacity is determined using Static Thermal Rating (STR) according to IEC 60287 [4,5], which assumes worst-case environmental and operating conditions. While this ensures operational safety, it underutilizes available capacity for most of the year and can result in oversizes and costly cable designs [6].

Dynamic Thermal Rating (DTR) offers an adaptive alternative to conventional STR by continuously adjusting cable ampacity according to real-time or forecasted environmental and operational conditions [7,8]. Extensive research on DTR for overhead transmission lines [9–12] has demonstrated its potential to unlock latent capacity by taking advantage of favorable weather conditions, thereby enhancing asset utilization and deferring costly reinforcements. In overhead applications, parameters such as wind speed, ambient temperature, and solar radiation have a noticeable impact on conductor ampacity. In contrast, the application of DTR to submarine HVAC cables is relatively recent, with research still emerging to address the distinct thermal environment of seabed installations and their unique operational constraints. Nonetheless, it is gaining importance as offshore renewable capacity expands, particularly in projects employing overplanting strategies [13]. Studies have

* Corresponding author.
Email address: mojtaba.moradisepahvand@tno.nl (M. Moradi-Sepahvand).

https://doi.org/10.1016/j.segan.2026.102263
Received 15 September 2025; Received in revised form 24 February 2026; Accepted 13 April 2026
Available online 27 April 2026

demonstrated that integrating DTR with accurate thermal models can increase export capacity, reduce curtailment, and postpone infrastructure upgrades [3,14,15]. These benefits are especially relevant for offshore systems with highly variable generation profiles, such as those combining overplanting with hybrid offshore solar–wind generation. A variety of modeling approaches have been proposed for implementing DTR in submarine cables. Physics-based methods, such as thermal–electrical equivalent (TEE) networks [16,17], strike a balance between computational tractability and modeling accuracy, making them suitable for integration into operational optimization frameworks. However, modeling three-core HVAC cables remains challenging due to the complexity of accurately capturing their coupled thermal and electrical behaviors [18]. Although adaptations of the TEE framework have been proposed to account for effective losses in long three-core HVAC cables [19], further refinement is still required to better capture thermal effects. Advanced sensing technologies, such as Distributed Temperature Sensing (DTS) using fiber optics [20,21], enable high-resolution temperature monitoring along the cable route, which can provide essential data for real-time DTR operation. Even with these advances, it is still challenging to model the complex thermal behavior of submarine cables, account for changes in seabed conditions, and validate simplified models against detailed simulations. In parallel with these modeling challenges, recent studies have examined DTR from broader system perspectives, including operational reliability, coordination, and system-level optimization under high renewable penetration [8,13,22–24]. In particular, the reliability impact of DTR under high wind penetration and frequency security constraints has been quantified, showing that dynamically adjustable thermal limits can enhance secure system operation in renewable-dominated networks [22]. DTR has also been integrated with additional flexibility resources, including battery storage, network topology optimization, and electric-vehicle scheduling, to enhance wind integration, reliability, and operational flexibility in onshore and microgrid contexts [23,24]. Nevertheless, for offshore HVAC export systems, the explicit integration of validated electro–thermal cable models into operational optimization frameworks remains limited.

This paper addresses these gaps by developing and validating an integrated electro–thermal–economic optimization framework that explicitly embeds a transient three-core cable model within a binary-free Optimal Power Flow (OPF) framework for OWF export systems under DTR operation. The framework:

1. Integrates a transient electro–thermal model of HVAC submarine cables with a binary-free Linear Programming (LP)-based dynamic OPF formulation;
2. Accounts for hourly wind generation, electricity market prices, and environmental variability;
3. Validates the simplified model against high-fidelity finite element simulations in COMSOL Multiphysics;
4. Incorporates realistic offshore scenarios, including overplanting and hybrid solar–wind generation;

The remainder of this paper is organized as follows: Section 2 introduces the modeling methodology, Section 3 presents the case studies with COMSOL model validation and DTR-based dynamic OPF numerical results, and Section 4 concludes with key findings and future research directions.

2. Methodology

2.1. Overview

In this section, a coupled electro-thermal and operational optimization framework for HVAC submarine export cables under DTR is developed. The thermal behavior is modeled via a TEE network using lumped thermal resistances and capacitances, while conductor, dielectric, sheath, and armor losses are represented as distributed heat sources. The resulting thermal dynamics are discretized using a backward Euler scheme [25] and embedded within a binary-free linear OPF formulation. Nonlinear I^2R loss terms are approximated through a lower-convex-envelope linearization [26], enabling computationally tractable optimization over long time horizons.

The methodology follows a structured progression. The physical cable configuration (Section 2.2) forms the basis of the TEE representation (Section 2.3), from which electrical losses and heat sources are derived (Section 2.4). These quantities are incorporated into a thermal state-space model (Section 2.5) to evaluate temperature evolution and limits (Section 2.6). The nonlinear loss expressions are subsequently linearized (Section 2.7), allowing their integration into the OPF formulations under STR and DTR constraints (Sections 2.8 and 2.9).

2.2. High-voltage submarine three-core XLPE cable

A three-core XLPE-insulated HVAC submarine export cable is considered (Fig. 1), including conductor, conductor screen, insulation, insulation screen and lead sheath, inner sheath, fillers, fiber-optic, binding tapes, armor bedding, armor, and outer serving. The OWF is connected to shore via a single export circuit. Transformers, J-tubes, and switchgear are assumed adequately rated and non-limiting. Note that junctions/splices are neglected (consistent with [13,14,27]) due to limited DTR-grade models.

2.3. Thermal–electrical equivalent (TEE) network

The TEE network provides a simplified approach to modeling transient heat transfer in submarine cables [14,28].

Analogy. Temperature (θ) maps to voltage, heat flow (W) to current, thermal resistance (T) to electrical resistance, and thermal capacitance (Q) to electrical capacitance (Fig. 2). This permits nodal heat-balance via Kirchhoff's current/voltage laws (KCL/KVL) [14].

Full and reduced ladder models. A full thermal ladder (Fig. 3) represents individual layers (conductor, insulation, lead, fillers, armor, jacket, soil) with T/Q elements [4,28]; a steady-state version (Fig. 4) opens capacitors. For DTR integration we adopt a reduced three-node model (Fig. 5) with equivalence [29]:

$$T_c = \frac{T_1}{3} \quad [\mathrm{K\cdot m/W}] \tag{1a}$$

$$T_{sh} = T_2 + T_3 \quad [\mathrm{K\cdot m/W}] \tag{1b}$$

$$Q_c = 3\cdot Q_{\mathrm{con}} + 3\cdot p\cdot Q_i \quad [\mathrm{J/m\cdot K}] \tag{1c}$$

$$Q_{sh} = (1-p)\cdot 3\cdot Q_i + \left(\frac{T_2+T_3}{T_2+T_3}\right)^2 \left(3\cdot Q_{\mathrm{shle}} + \frac{Q_f}{2}\right) + \left(\frac{T_3}{T_2+T_3}\right)^2 \left(\frac{Q_f}{2} + Q_a + p'\cdot Q_j\right) \quad [\mathrm{J/m\cdot K}] \tag{2}$$

where T_c denotes the per-core equivalent thermal resistance of the three identical conductors (each with thermal resistance T_1), and T_{sh} is the equivalent thermal resistance of the sheath region, consisting of the lead sheath-to-armor (T_2) and armor-to-soil (T_3) resistances. In (1c), Q_c is the effective thermal capacitance of the conductor region, consisting of the conductor capacitance Q_{con} and insulation thermal capacitance Q_i. Similarly, Q_{sh} in (2) represents the thermal capacitance of the sheath region. It accounts for the insulation capacitance, the lead sheath capacitance around each core Q_{shle}, as well as the capacitances of the filler (Q_f), armor (Q_a), and outer jacket (Q_j). The thermal resistance ratio in the second term of (2) evaluates to unity for the present reduced formulation but is retained to preserve traceability between the full thermal ladder and the simplified three-node model. Note that p and p' are Van Wormer's coefficients based on [29] expressed in (15) to (17). Thermal resistances T_1 to T_3 are expressed as:

$$T_1 = \frac{\rho_i}{2\pi}\ln\left(\frac{D_I}{D_c}\right) \quad [\mathrm{K\cdot m/W}], \tag{3}$$

$$T_2 = \frac{\rho_k}{6\pi} G(X_k) \quad [\mathrm{K\cdot m/W}], \quad X_k = \frac{T B_{tck}}{D_k}, \tag{4}$$

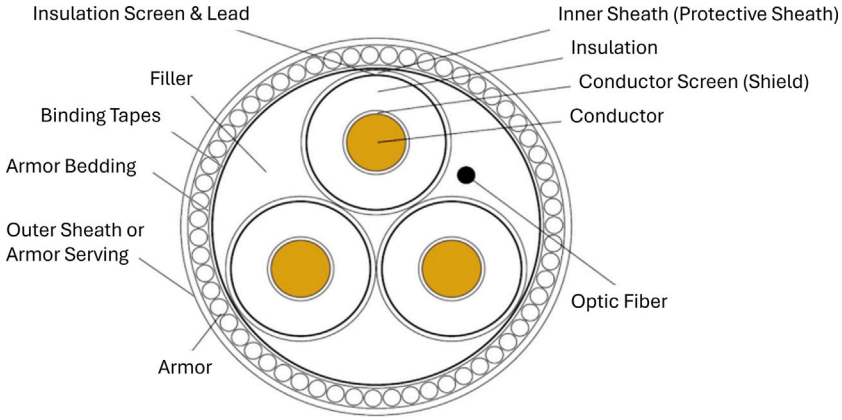

Fig. 1. General structure of a high voltage three-core XLPE submarine cable.

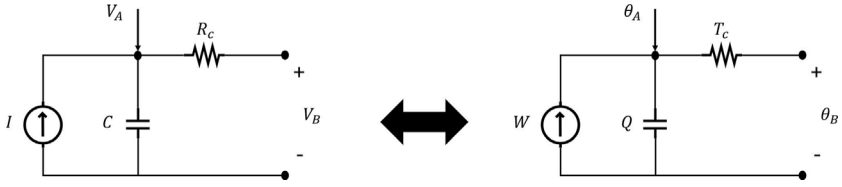

Fig. 2. The equivalent electrical circuit for heat transfer modeling.

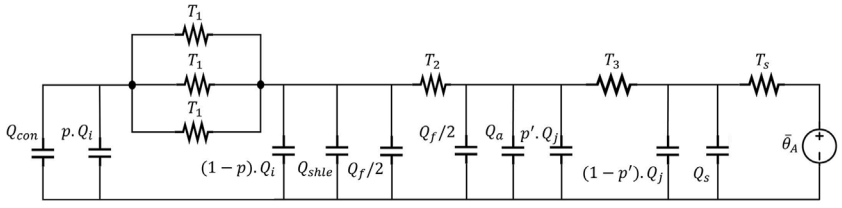

Fig. 3. Full thermal ladder equivalent electrical circuit for a three-core XLPE submarine cable.

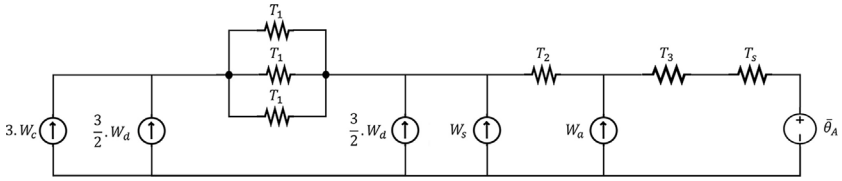

Fig. 4. Steady-state thermal ladder equivalent electrical circuit showing distributed losses across cable layers for a three-core XLPE submarine cable.

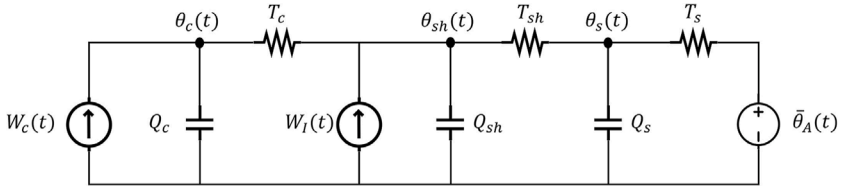

Fig. 5. Final simplified thermal ladder equivalent electrical circuit considering losses for a three-core XLPE submarine cable.

$$T_3 = \frac{\rho_j}{2\pi} \ln\left(1 + \frac{2 \cdot AS_{tck}}{D_a + 2 \cdot A_{tck}}\right) \quad [\mathrm{K \cdot m/W}] \tag{5}$$

where ρ_i, ρ_k, ρ_j are the thermal resistivities of the insulation, sheath, and armor materials, respectively, expressed in unit of K·m/W. D_c is the conductor diameter, D_l is the lead sheath inner diameter, D_k is the sheath outer diameter, and D_a is the armor internal diameter, all expressed in meter m. TB_{tck} is the thickness between inner sheath and armor; A_{tck} and AS_{tck} are the thicknesses of the armor and armor serving; $G(X_k)$ is a dimensionless geometric factor as defined in [5,14], dependent on the normalized sheath thickness X_k. Soil-related terms are:

$$T_s = \frac{1}{2\pi}\rho_s \ln\left(\frac{2L}{D_j} + \sqrt{\left(\frac{2L}{D_j}\right)^2 - 1}\right) \quad [\mathrm{K \cdot m/W}], \tag{6}$$

$$Q_s = \frac{\pi}{4}\psi_s\left(L^2 - D_j^2\right) + (1-p')\,Q_j \quad [\mathrm{J/m\cdot K}] \tag{7}$$

where ρ_s is the thermal resistivity of the surrounding soil; D_j is the outer diameter of the cable jacket; L is the burial depth of the cable below seabed level; ψ_s is the volumetric heat capacity of the soil; Q_s represents the soil's effective thermal capacitance.

Ambient (seabed) temperature. The ambient node uses seabed temperature $\bar{\theta}_A(t)$. Considering only sea-surface temperature $\theta_{\mathrm{surf}}(t)$, a 1-D vertical conduction estimation is adopted:

$$\bar{\theta}_A(t) = \theta_{\mathrm{surf}}(t) - \phi_{\mathrm{geo}}\,\rho_{sw}\,H, \tag{8}$$

where $\phi_{\mathrm{geo}}(\mathrm{W/m^2})$, $\rho_{sw}(\mathrm{K.m/W})$, and H are geothermal flux, seawater thermal resistivity, and water depth, respectively.

Layer thermal capacitances. Thermal capacity of each layer can be defined as:

$$Q_{\mathrm{con}} = \psi_{\mathrm{con}}\cdot A_{\mathrm{con}}, \quad [\mathrm{J/m\cdot K}] \tag{9}$$

$$Q_i = \frac{\pi}{4}\psi_i(D_i^2 - D_c^2), \quad [\mathrm{J/m\cdot K}] \tag{10}$$

$$Q_{\mathrm{shle}} = \frac{\pi}{4}\psi_{\mathrm{shle}}(D_{ol}^2 - D_i^2), \quad [\mathrm{J/m\cdot K}] \tag{11}$$

$$Q_f = \frac{\pi}{4}\psi_f(D_a^2 - D_{ol}^2), \quad [\mathrm{J/m\cdot K}] \tag{12}$$

$$Q_a = \frac{\pi}{4}\psi_a\cdot NAW\cdot(A_{tck})^2, \quad [\mathrm{J/m\cdot K}] \tag{13}$$

$$Q_j = \frac{\pi}{4}\psi_j\left(D_j^2 - (D_j - 2\cdot AS_{tck})^2\right) \quad [\mathrm{J/m\cdot K}] \tag{14}$$

Van Wormer coefficients are [29]:

$$p = \frac{1}{2\ln\left(\frac{D_i}{ED_c}\right)} - \frac{1}{\left(\frac{D_i}{ED_c}\right)^2 - 1}, \tag{15}$$

$$p' = \frac{1}{2\ln\left(\frac{D_j}{D_a+2A_{tck}}\right)} - \frac{1}{\left(\frac{D_j}{D_a+2A_{tck}}\right)^2 - 1}, \tag{16}$$

$$ED_c = D_l\cdot\exp\left(-\frac{2\pi T_c}{\rho_i}\right) \tag{17}$$

Here D_i denotes the insulation outer diameter, D_{ol} the lead sheath outer diameter, NAW the number of armor wires, ED_c the equivalent conductor diameter in Van Wormer's formulation, and ψ the volumetric heat capacity of the respective material. Note that in (17), T_c represents the per-core thermal resistance used in the equivalent single-core formulation, as defined in (1a).

Material data. Thermal resistivity (ρ) and volumetric heat capacity (ψ) are defined in Table 1 [5,13,14,30,31].

Table 1
Thermal resistivity and heat capacity of materials.

Material	ρ [K·m/W]	ψ [$\times 10^6$ J/m^3·K]
Copper	–	3.46
Aluminum	–	2.46
Lead / Lead-alloy (Pb)	–	1.47
Armor (Steel wires)	–	3.80
Polyethylene (PE)	3.5	2.40
Cross-linked PE (XLPE)	3.5	2.40
Filler (PE)	3.5	2.40
Polypropylene (PP)	10	1.80
Seabed soil	0.9	2.18

2.4. Electrical losses and heat sources

Total internal heat per unit length ([W/m]) is defined as:

$$W_I(t) = W_s(t) + W_a(t) + 3W_d = \left(\lambda_1+\lambda_2\right)W_c(t) + 3W_d \tag{18}$$

The per-phase conductor AC resistance at 90 °C (Ω/m) is expressed as a function of the copper DC resistivity ρ_c at 20 °C, the conductor cross-sectional area A_{con}, and the temperature coefficient of resistivity α_c:

$$R_{ac} = \left(\rho_c\frac{1}{A_{con}}\left[1+\alpha_c(\theta_c^{\max}-20)\right]\right)\left(1+Y_s+Y_p\right) \tag{19}$$

where Y_s and Y_p denote the skin and proximity effect factors, respectively, as defined in [4,14].

The conductor and dielectric losses per unit length (W/m) are then given by [4,13]:

$$W_c(t) = 3\,R_{ac}\,I(t)^2,\ W_d = \omega C_c V_{ph}^2\tan\delta\times 10^{-9} \tag{20}$$

$$C_c = \frac{2.5}{18\ln(D_i/D_c)}\ [\mu\mathrm{F/km}] \tag{21}$$

where $\omega = 2\pi f$ is the angular frequency of the system, f is the power system frequency (Hz), and V_{ph} is the phase voltage of the cable (V), and C_c and $\tan\delta$ represent the cable capacitance per unit length and dielectric losses, respectively. Lead-sheath and armor loss factors (λ_1, λ_2) for SL-type three-core cables are [4,29,32–35]:

$$\lambda_1 = \frac{R_s}{R_{ac}}\frac{1.5}{1+\left(\frac{R_s}{X_{LS}}\right)^2},\quad X_{LS} = \omega\ln\left(\frac{2D_k}{D_k - 2S_{tck} - L_{tck}}\right)\times 2\times 10^{-7}$$
$$\lambda_2 = 1.23\frac{R_a}{R_{ac}}\left(\frac{2D_{co}}{D_{aa}}\right)^2\frac{1}{\left(2.77R_a\frac{10^6}{2\pi f}\right)^2+1}(1-\lambda_1) \tag{22}$$

In (22), $D_{co} = D_k/\sqrt{3}$ is the equivalent conductor spacing, and $D_{aa} = D_a + A_{tck}$ is the effective armor diameter. The sheath and armor resistances (Ω/m) are:

$$R_s = \frac{\rho_s}{\frac{\pi}{4}\left(D_{ol}^2 - D_l^2\right)}\left(1+\alpha_s(\theta_{sh}^{max}-20)\right),$$
$$R_a = \frac{\rho_a}{\frac{\pi}{4}\left((D_j - 2\cdot AS_{tck})^2 - D_a^2\right)}\left(1+\alpha_a(\theta_a^{max}-20)\right) \tag{23}$$

where θ_{sh}^{max} and θ_a^{max} are the lead sheath and armor steady-state temperatures.

2.5. Thermal state-space and discretization

Let $\theta_c, \theta_{sh}, \theta_s$ denote conductor, inner sheath, and soil node temperatures. The continuous dynamics, derived from the equivalent electrical circuit in Fig. 5 using KCL, are formulated as follows:

$$\frac{d}{dh}\begin{bmatrix}\theta_c(h)\\ \theta_{sh}(h)\\ \theta_s(h)\end{bmatrix} = A\begin{bmatrix}\theta_c(h)\\ \theta_{sh}(h)\\ \theta_s(h)\end{bmatrix} + \begin{bmatrix}\frac{W_c(h)}{Q_c}\\ \frac{W_I(h)}{Q_{sh}}\\ \frac{\theta_A(h)}{Q_sT_s}\end{bmatrix}, \tag{24}$$

$$A = \begin{bmatrix}-\frac{1}{Q_cT_c} & \frac{1}{Q_cT_c} & 0\\ \frac{1}{Q_{sh}T_c} & -\left(\frac{1}{Q_{sh}T_c}+\frac{1}{Q_{sh}T_{sh}}\right) & \frac{1}{Q_{sh}T_{sh}}\\ 0 & \frac{1}{Q_sT_{sh}} & -\left(\frac{1}{Q_sT_{sh}}+\frac{1}{Q_sT_s}\right)\end{bmatrix}$$

The discrete-time state-space formulation, obtained via the Backward Euler method [25] with a step size $\Delta h = 1$ h, is expressed as:

$$\theta_{h+\Delta h} = (I - \Delta h\cdot A)^{-1}\left(\theta_h + \Delta h\cdot B_{h+\Delta h}\right), \tag{25}$$

which can be expanded component-wise as in (42)–(44). Note that the hourly discretization aligns with the temporal resolution of market-based dispatch and is consistent with the multi-hour thermal time

constants of submarine cables. The Backward Euler scheme is adopted for its unconditional stability in long-horizon simulations; any numerical damping of very fast transients is negligible relative to the dominant multi-hour thermal dynamics.

2.6. Thermal limits

Maximum admissible steady-state temperatures, based on the STR maximum current $I_{\max}$ and an ambient temperature of 20 °C, are calculated as:

$$\theta_c^{\max} = T_c W_c^{\max} + (T_{sh} + T_s)\left[W_c^{\max}(1+\lambda_1+\lambda_2) + 3W_d\right] + 20\,^\circ\mathrm{C}, \tag{26}$$

$$\theta_{sh}^{\max} = \theta_c^{\max} - T_c W_c^{\max}, \tag{27}$$

$$\theta_s^{\max} = \theta_{sh}^{\max} - T_{sh}\left[W_c^{\max}(1+\lambda_1+\lambda_2) + 3W_d\right] \tag{28}$$

Here, $W_c^{\max} = 3R_{ac}I_{\max}^2$ is the maximum STR current loss, and $\theta_c^{\max} = 90\,^\circ\mathrm{C}$. During operation, the following constraints are enforced:

$$\theta_c(h) \le \theta_c^{\max},\ \theta_{sh}(h) \le \theta_{sh}^{\max},\ \theta_s(h) \le \theta_s^{\max} \quad \forall h \in \Omega_H \tag{29}$$

2.7. Loss linearization via lower convex envelope

Let P_h denote the exported active power (MW) in the cable, and define $\Psi_h \approx P_h^2$. The three-phase line losses, with total per-phase resistance R [Ω] (R_{ac} [Ω/m] × *Cable Length* [m]) and line-to-line voltage V [kV], are:

$$\mathrm{Loss}_h = 3RI_h^2 = 3R\frac{\Psi_h}{(\sqrt{3}V)^2}, \quad \forall h \in \Omega_H \quad [\mathrm{MW}] \tag{30}$$

To maintain linearity, the quadratic term Ψ_h is approximated from below using a lower convex envelope constructed with G tangents [26]:

$$\Psi_h \ge 2\pi_g P_h - \pi_g^2 \quad \forall h \in \Omega_H, g \in \{1,\dots,G\} \tag{31}$$

$$\pi_g = \frac{g-1}{G-1}P^{\max} \quad \forall g \in \{1,\dots,G\} \tag{32}$$

2.8. OPF with STR limits

A DC OPF is formulated between the offshore substation (S) and the point of common coupling (PCC) onshore. The corresponding mathematical formulation is summarized below.

Sets and Indices:

Ω_T, Ω_H: sets of wind turbines indexed by i, and hourly time indices h

Parameters:

$P_{i,h}^{\mathrm{Turb}}$, P_h^{Solar}: available wind power of turbine i and total solar generation at hour h (MW)

V: line-to-line voltage (kV)

X, R: cable reactance and per-phase resistance (Ω)

$P^{\max}$: export capacity limit under STR (MW)

$C_{\mathrm{loss}}, C_{\mathrm{curt}}$: loss and curtailment cost coefficients (€/MWh)

MP_h: electricity market price at hour h (€/MWh)

Decision Variables:

P_h: exported active power (MW)

Ψ_h: auxiliary loss variable (MW^2)

$W_{i,h}^{\mathrm{Curt}}$, S_h^{Curt}: wind and solar curtailment (MW)

δ_h^S: offshore substation voltage angle (rad)

θ_h^c, θ_h^{sh}, θ_h^s: conductor, inner sheath, and soil node temperature at hour h (°C), introduced in the DTR formulation

The OPF objective maximizes net profit (equivalently, minimizes losses and curtailment penalty costs, i.e., C_{loss} and C_{curt}):

$$\min \sum_{h\in\Omega_H}\Bigg[\underbrace{\frac{3\Psi_h}{(\sqrt{3}V)^2}RC_{\mathrm{loss}}}_{\text{Loss cost}} + \underbrace{\Big(\big(\sum_{i\in\Omega_T} W_{i,h}^{\mathrm{Curt}}\big) + S_h^{\mathrm{Curt}}\Big)C_{\mathrm{curt}}}_{\text{Curtailment cost}}\Bigg]$$

$$- \sum_{h\in\Omega_H}\mathrm{MP}_h\left(P_h - \frac{3\Psi_h}{(\sqrt{3}V)^2}R\right) \tag{33}$$

$$\text{s.t.} \quad P_h = \sum_{i\in\Omega_T}\left(P_{i,h}^{\mathrm{Turb}} - W_{i,h}^{\mathrm{Curt}}\right) + P_h^{\mathrm{Solar}} - S_h^{\mathrm{Curt}}, \quad \forall h \in \Omega_H \tag{34}$$

$$P_h = \frac{V^2}{X}\left(\delta_h^S - \delta_h^{PCC}\right), \quad \forall h \in \Omega_H \tag{35}$$

$$\delta_h^{PCC} = 0, \quad -\tfrac{\pi}{3} \le \delta_h^S \le \tfrac{\pi}{3}, \quad \forall h \in \Omega_H \tag{36}$$

$$\frac{3\Psi_h}{(\sqrt{3}V)^2}R \ \le\ P_h, \quad \forall h \in \Omega_H \tag{37}$$

$$P_h + \frac{3\Psi_h}{(\sqrt{3}V)^2}R \ \le\ P^{\max} \quad \forall h \in \Omega_H \tag{38}$$

$$\text{constraints} \quad (31)-(32) \tag{39}$$

The quadratic loss term P_h^2 is replaced by the auxiliary variable Ψ_h according to the lower–convex–envelope formulation introduced in (Section 2.7) (i.e., (30)–(32)).

2.9. OPF with DTR constraints

The DTR-based OPF adopts the same objective function (33) as in the STR case and remains subject to the power-balance constraints (34)–(36) and the loss linearization constraints (31)–(32). The key addition is the incorporation of hourly thermal recursions derived from (25), together with the temperature limits (29), formulated as follows:

$$\text{Objective: (33)} \tag{40}$$

$$\text{s.t. constraints (34)} - (36), (31) - (32), (29) \tag{41}$$

$$\theta_{h+1}^c = \frac{Q_cT_c}{Q_cT_c+1}\theta_h^c + \frac{1}{Q_cT_c+1}\theta_{h+1}^{sh} + \frac{T_c}{Q_cT_c+1}W_{h+1}^c \quad \forall h \in \Omega_H \setminus \{H\} \tag{42}$$

$$\theta_{h+1}^{sh} = \frac{Q_{sh}T_{sh}T_c}{Q_{sh}T_{sh}T_c+(T_{sh}+T_c)}\theta_h^{sh} + \frac{T_{sh}}{Q_{sh}T_{sh}T_c+(T_{sh}+T_c)}\theta_{h+1}^c + \frac{T_c}{Q_{sh}T_{sh}T_c+(T_{sh}+T_c)}\theta_{h+1}^s + \frac{T_{sh}T_c}{Q_{sh}T_{sh}T_c+(T_{sh}+T_c)}W_{h+1}^I \quad \forall h \in \Omega_H \setminus \{H\} \tag{43}$$

$$\theta_{h+1}^s = \frac{Q_sT_{sh}T_s}{Q_sT_{sh}T_s+(T_{sh}+T_s)}\theta_h^s + \frac{T_s}{Q_sT_{sh}T_s+(T_{sh}+T_s)}\theta_{h+1}^{sh} + \frac{T_{sh}}{Q_sT_{sh}T_s+(T_{sh}+T_s)}\bar{\theta}_{h+1}^A \ \forall h \in \Omega_H \setminus \{H\} \tag{44}$$

with initial steady-state conditions $\theta_0^c = \theta_0^{sh} = \theta_0^s = \bar{\theta}_0^A$.

The heat inputs W^c and W^I follow (18)–(21) and (30). Note that all diameters are expressed in meters. Resistances R_{ac}, R_s, R_a are per phase in Ω/m. For hourly discretization, Q must be in Wh/(m · K), obtained by dividing by 3600 from J/(m · K).

3. Case study, model validation & numerical results

3.1. Case study

The case study focuses on the Hollandse Kust West Beta (HKWB) offshore wind farm, which is scheduled to become operational in 2025 with an installed capacity of up to 700 MW [36]. The full project comprises 108 wind turbines of 14 MW each, connected through two parallel 220 kV three-core AC export cable circuits. For this study, a single export circuit is considered, corresponding to 54 turbines and a baseline installed capacity of 756 MW.

Two scenarios are considered: (**i**) an **Overplanting scenario**, where up to 16 additional turbines raise the capacity to 980 MW, enabling the assessment of DTR under expansion; and (**ii**) a **Hybrid scenario**, where 5–50 MW of floating solar is co-located with HKWB, reflecting ongoing SolarDuck–RWE pilots [37] and allowing the exploration of how DTR can facilitate the use of existing export cables in future hybrid configurations.

The export cable under study is a standard XLPE-insulated 3 × 1000 mm^2 copper HVAC design [38], with a rated current of 950 A at

Table 2
Specifications of the 3×1000 mm^2 HVAC XLPE-insulated submarine export cable.

Electrical		Geometry	
Parameter	Value	Parameter	Value
Voltage level	220 kV	Burial depth	1 m
Frequency	50 Hz	D_c	38.6 mm
Conductor	Copper	D_i	88 mm
Nominal Cross-sectional Area	1000 mm^2/core	D_l	92.2 mm
Real Cross-sectional Area	1170.21 mm^2/core	D_{ol}	99.4 mm
Rated current	950 A	D_k	104.6 mm
DC R (20 °C)	1.43×10^{-5} Ω/m	D_a	227 mm
AC R (90 °C)	2.34×10^{-5} Ω/m	D_j	245 mm
Reactance	1.19×10^{-4} Ω/m	TB_{tck}	0.81 mm
Lead resistivity	22×10^{-8} Ωm	A_{tck}	5 mm
Steel resistivity	15.7×10^{-8} Ωm	AS_{tck}	4 mm
		S_{tck}	2.6 mm
		L_{tck}	3.6 mm
		NAW	110

Table 3
Maximum Steady-State Temperatures: Analytical model vs. COMSOL.

Layer	Analytical (°C)	COMSOL (°C)	Relative error (%)
Core ($\theta_c^{\max}$)	90.00	89.80	0.22
Inner Sheath ($\theta_{sh}^{\max}$)	79.94	79.47	0.59
Soil at Serving ($\theta_s^{\max}$)	67.55	67.43	0.18

220 kV. The main specifications of the cable are summarized in Table 2. The analysis incorporates 2023 historical offshore wind production data and electricity market prices from the Netherlands [39], as well as ambient seabed temperatures obtained from KNMI [40]. For the hybrid case, solar generation profiles are derived from aggregated national solar production datasets (2023) [39] and scaled to the assumed floating PV capacity, given the current absence of operational offshore PV datasets in the Netherlands.

3.2. Model validation using FEM

To assess the accuracy of the proposed DTR mathematical model, its results are benchmarked against finite element simulations carried out in COMSOL Multiphysics. This approach enables detailed multi-physics modeling of submarine power cables, including heat transfer in multiple layers and the surrounding soil [41]. The comparison is performed for both steady-state and transient operating conditions.

3.2.1. Steady-state validation

The developed analytical model, based on the formulations in (1a)–(30), yields the maximum admissible steady-state temperatures of $\theta_c^{\max} = 90.0\,°C$ (core), $\theta_{sh}^{\max} = 79.94\,°C$ (inner sheath), and $\theta_s^{\max} = 67.55\,°C$ (soil at serving point), as summarized in Table 3. The same cable is modeled in the FEM environment. The steady-state simulation under rated current produces maximum temperatures of 89.80 °C, 79.47 °C, and 67.43 °C, respectively, as reported in Table 3. The relative deviations remain below 0.6%, quantitatively confirming the high steady-state accuracy of the proposed electro–thermal formulation. The spatial temperature distribution across cable layers and soil is illustrated in Fig. 6. The close agreement between the analytical and numerical results further validates the accuracy of the developed electro–thermal model. Note that the analytical method is slightly conservative due to the safety margins embedded in the mathematical formulations.

3.2.2. Transient validation

A 3200 h stepwise power profile (four 800 h steps) was applied to assess transient accuracy. The analytical model (Fig. 7) illustrates the rapid response of the core (blue solid line) to load variations, whereas the sheath (red dashed line) and soil (green dotted line) exhibit slower dynamics due to their higher thermal inertia. In the second loading step, the power exceeds the STR limit; however, the core temperature surpasses 90 °C only briefly.

The same profile was simulated in the FEM environment. The comparison in Fig. 8 demonstrates strong agreement in both trend and magnitude. The analytical temperatures are slightly higher (i.e., more conservative) than the numerical results, which is expected since the mathematical formulation is based on IEC assumptions and incorporates inherent safety margins [4,5,28]. This conservative approach is advantageous in planning and operations, as it guarantees compliance with thermal limits under uncertain conditions. Over the full 3200 h transient profile, the mean absolute error (MAE) and root mean square error (RMSE) of the conductor temperature between the analytical model and COMSOL are 3.35 °C and 3.64 °C, respectively. Overall, the close match validates the developed electro-thermal model, whose efficiency makes it well suited for large-scale studies, DTR-aware OPF, and real-time offshore operations.

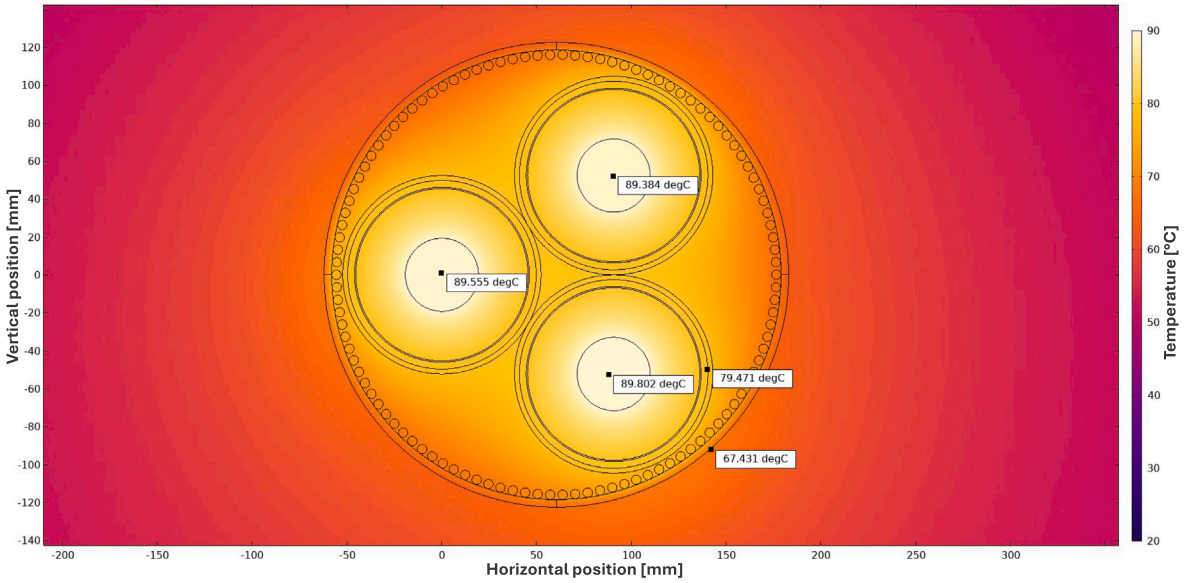

Fig. 6. Steady-state temperature distribution of cable layers and soil (COMSOL).

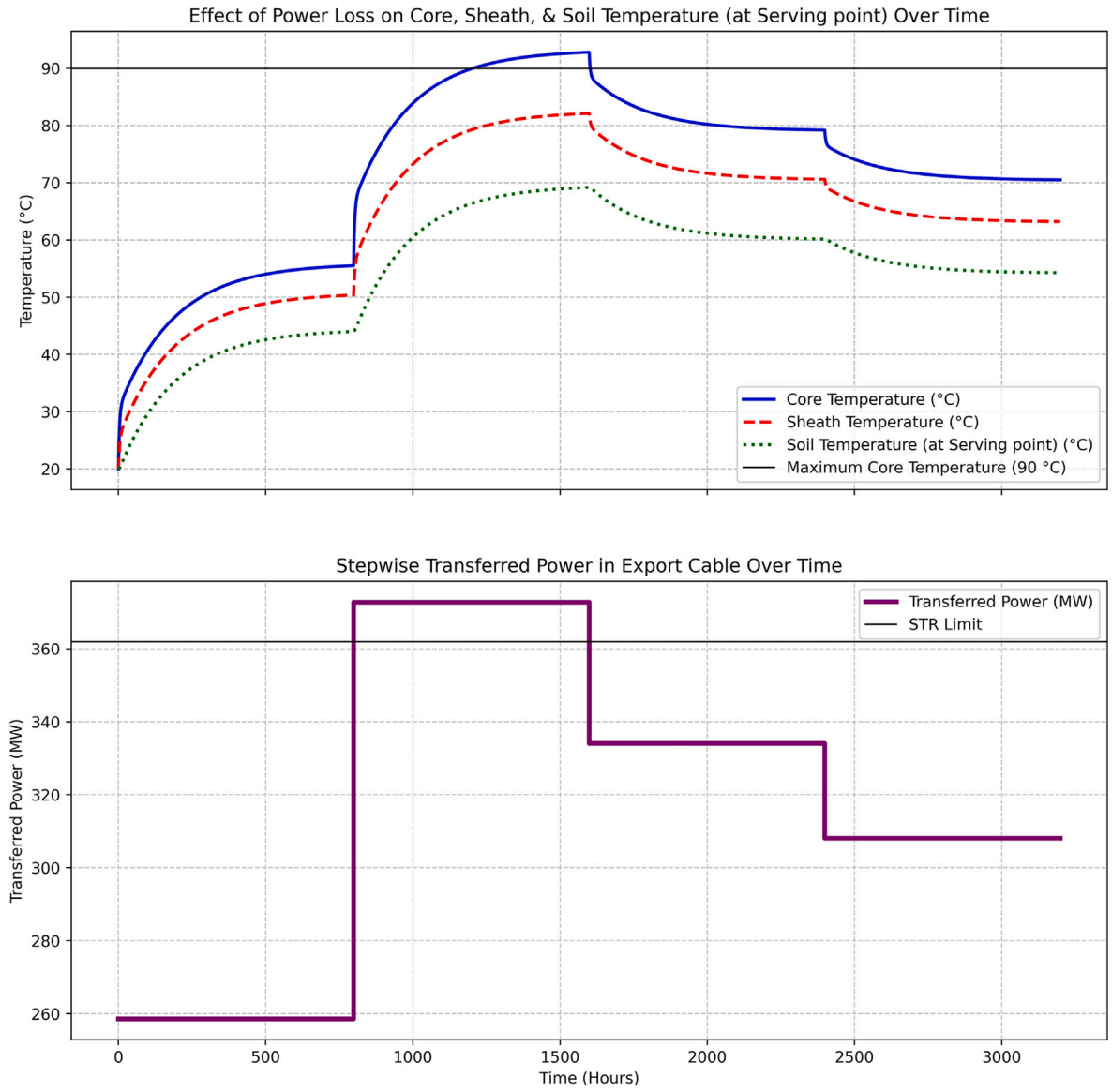

Fig. 7. Stepwise power transfer: analytical model predictions of core, sheath, and soil temperatures over 3200 h.

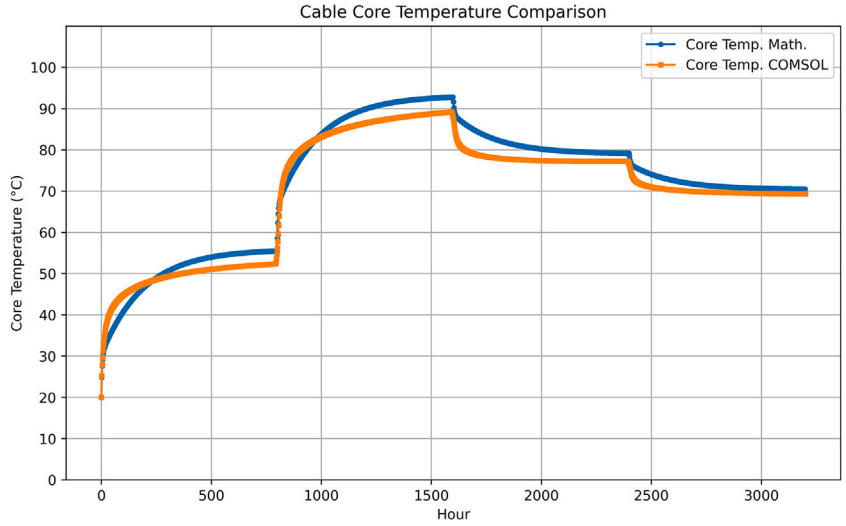

Fig. 8. Comparison of core temperature dynamics between analytical (Math.) and numerical (COMSOL) methods under stepwise power transfer.

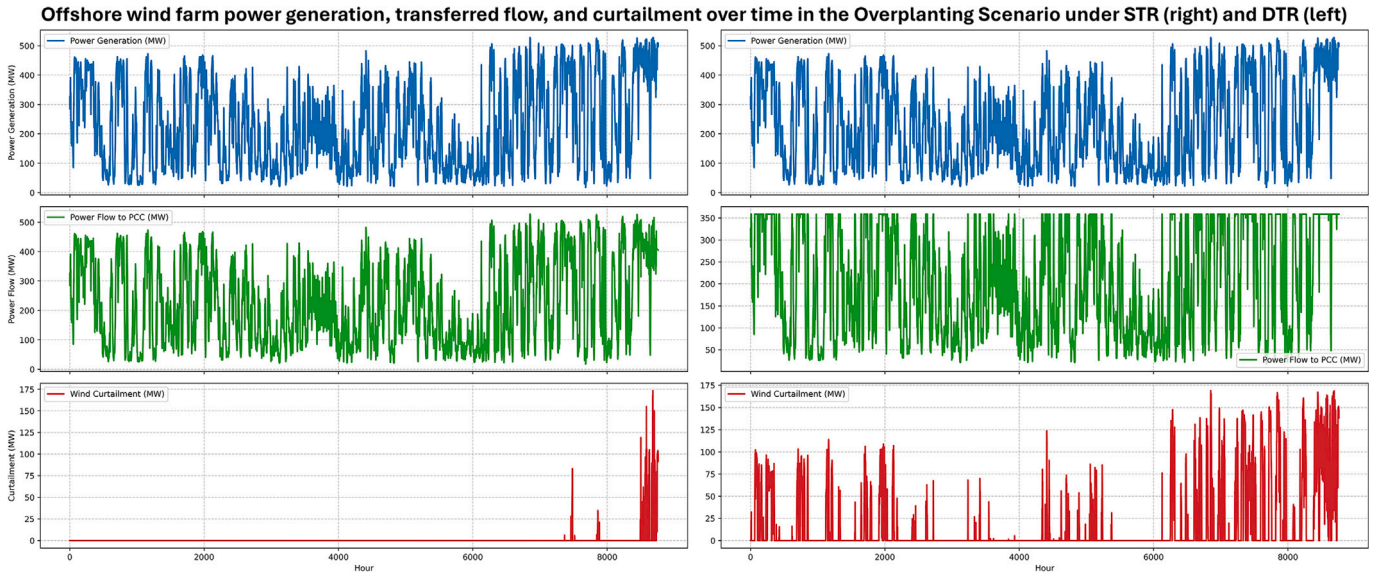

Fig. 9. Comparison of power flow, generation, and curtailment over time in the overplanting scenario under STR (right) and DTR (left).

Table 4
Economic Summary of Overplanting Scenario: STR vs. DTR.

Metric	STR	DTR
Curtailment (GWh)	150.66	11.07
Total Revenue (M€)	156.99	166.76

3.3. Numerical results: overplanting scenario

3.3.1. Overplanting under STR

The DC OPF optimization with STR, presented by (33)-(39), is applied to the HKWB case study. In the overplanting scenario, 16 additional turbines raise the installed capacity to 980 MW. As shown on the right side of Fig. 9, although generation potential increases, transmission through the cable is constrained by the STR limit, leading to substantial curtailment. Table 4 summarizes the financial outcome, with a total revenue of 156.99 M€and 150.66 GWh of curtailed wind energy. Avoiding such curtailed energy under STR would require reinforcing the export system with an additional 300 mm^2 cable, at an estimated investment of 70.6 M€ (based on the cost estimation of Smith and Doe [42]), which highlights the inefficiency of static design.

3.3.2. Overplanting under DTR

With DTR, cable loading adapts to real-time thermal and environmental conditions, as determined by the formulations in (40)–(44). As shown on the left side of Fig. 9, this flexibility reduces curtailment and enables higher power export compared to STR. Curtailment falls from 150.66 GWh to just 11.1 GWh (≈ 93% reduction), while revenue increases to 166.76 M€ (Table 4).

3.3.3. STR vs. DTR comparison

Under STR, significant curtailment and costly reinforcement (≈70.6 M€) are required to fully exploit export capacity. By contrast, DTR, as reported in Table 4, achieves higher revenues with drastically

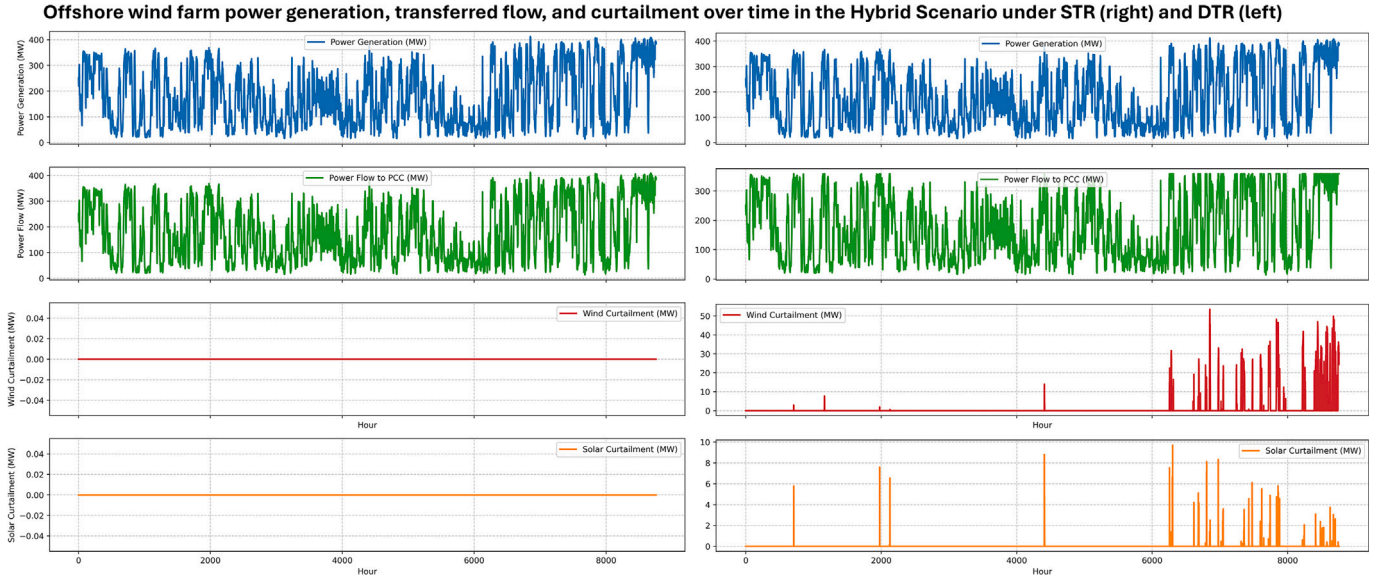

Fig. 10. Comparison of power flow, generation, and curtailment over time in the hybrid scenario under STR (right) and DTR (left).

Table 5
Economic Summary of Hybrid Scenario: STR vs. DTR.

Metric	STR	DTR
Curtailment (GWh)	10.32	0
Total Revenue (M€)	130.43	131.02

reduced curtailment, all without additional infrastructure. This demonstrates that DTR is not only technically effective but also a cost-efficient and sustainable alternative to conventional reinforcement strategies.

3.4. Numerical results: hybrid scenario

3.4.1. Hybrid operation under STR

In the hybrid case, up to 50 MW of floating solar is co-located with HKWB, sharing the same export cable. The solar production profile is based on scaled national generation data, as described previously. As shown on the right side of Fig. 10, solar generation coincides with wind output during midday, raising export peaks and leading to both wind and solar curtailment. Over the year, curtailment amounts to 10.32 GWh, with total revenue of 130.43 M€ (Table 5).

3.4.2. Hybrid operation under DTR

With DTR, the export cable adapts to real-time thermal conditions, allowing full utilization of both wind and solar output. As shown on the left side of Fig. 10, curtailment is eliminated, while revenues increase to 131.02 M€ (Table 5).

3.4.3. STR vs. DTR comparison

Under STR, hybrid operation suffers from renewable energy curtailment and profitability is limited. By contrast, DTR eliminates curtailment, improves revenue, and achieves higher utilization of the existing cable without reinforcements.

4. Conclusion

This study has presented a comprehensive framework for integrating Dynamic Thermal Rating (DTR) into the operation and economic optimization of offshore renewable energy systems. A physics-informed electro-thermal model was developed and validated against high-fidelity numerical simulations in COMSOL, demonstrating strong agreement across both steady-state and transient conditions. The validated model was then embedded into a dynamic optimal power flow (OPF) formulation to enable temperature-aware cable loading decisions that reflect real-time thermal and market conditions. Application to the Hollandse Kust West Beta (HKWB) offshore wind farm under overplanting and hybrid wind–solar scenarios demonstrated the significant value of DTR. In the overplanting case, curtailment was reduced by about 93% (from 150.66 GWh under static thermal rating (STR) to 11.07 GWh under DTR), while revenue increased from 156.99 M€ to 166.76 M€, without additional reinforcement costs. In the hybrid case, DTR eliminated the 10.32 GWh of renewable curtailment observed under STR, raising revenue from 130.43 M€ to 131.02 M€. These results confirm that DTR not only enhances the technical utilization of existing export infrastructure but also provides a cost-effective and sustainable alternative to conventional reinforcement strategies.

In summary, this study has shown that well-modeled DTR offers a scalable, robust, and cost-effective solution to improve offshore grid flexibility, minimize renewable curtailment, and maximize transmission asset utilization. At the same time, the analysis is limited by its focus on a single cable–wind farm configuration and simplified modeling assumptions. Future work should include validation of the approach on more varied offshore systems, exploration of real-time implementation, investigation of the integration of advanced short-term wind power forecasting to enhance dispatch decisions under renewable variability, consideration of coordination with flexible resources such as storage and hydrogen electrolysers, and analysis of the long-term effect of DTR-induced thermal cycling on cable life using insulation aging models.

CRediT authorship contribution statement

Mojtaba Moradi-Sepahvand: Writing – original draft, Visualization, Validation, Supervision, Software, Project administration, Methodology, Investigation, Funding acquisition, Formal analysis, Conceptualization. **Farzad Nasirpour:** Writing – review & editing, Visualization, Validation, Software, Methodology.

Declaration of competing interest

The authors declare that they have no known competing financial interests or personal relationships that could have appeared to influence the work reported in this paper.

Acknowledgements

This project has received funding from the Ideation Challenge Competition 2025 of the TNO Energy and Materials Transition (EMT) Unit. The authors also gratefully acknowledge the support provided by the Wind Energy Department of the TNO EMT Unit.

Data availability

Data will be made available on request.

References

[1] C. Walsh, D. Fraile, Offshore wind in Europe - key trends and statistics 2019 (windeurope). 2020. https://windeurope.org/wp-content/uploads/files/about-wind/statistics/WindEurope-Annual-Offshore-Statistics-2019.pdf. [Online]. Available: https://windeurope.org/wp-content/uploads/files/about-wind/statistics/WindEurope-Annual-Offshore-Statistics-2019.pdf.
[2] International Energy Agency, Net zero by 2050: a roadmap for the global energy sector, 2021, available: https://www.iea.org/reports/net-zero-by-2050.
[3] S.H.H. Kazmi, N. Viafora, T.S. Sørensen, T.H. Olesen, B.C. Pal, J. Holbøll, Offshore windfarm design optimization using dynamic rating for transmission components, IEEE Trans. Power Syst. 37 (3) (2021) 1820–1830.
[4] International Electrotechnical Commission, IEC 60287-1-1:2006 Electric Cables—Calculation of the Current Rating—Part 1-1: Current Rating Equations (100% Load Factor) and Calculation of Losses—General, International Electrotechnical Commission, Geneva, Switzerland, 2006.
[5] International Electrotechnical Commission (IEC), IEC 60287-2-1: Electric Cables – Calculation of the Current Rating – Part 2-1: Thermal Resistance – General Equations and Method for Cables with a Surface of Known Thermal Resistance, International Electrotechnical Commission (IEC), 2015.
[6] S. Karimi, P. Musilek, A.M. Knight, Dynamic thermal rating of transmission lines: a review, Renew. Sustain. Energy Rev. 91 (2018) 600–612.
[7] P. Wang, L. Kang, Z. Xu, W. Zhou, S. Bao, Z. Wu, Y. Hao, G. Liu, Dynamic thermal analysis for underground cables under continuously fluctuant load considering time-varying van wormer coefficient, Electr. Power Syst. Res. 199 (2021) 107395.
[8] C.-M. Lai, J. Teh, Comprehensive review of the dynamic thermal rating system for sustainable electrical power systems, Energy Rep. 8 (2022) 3263–3288.
[9] B.P. Bhattarai, J.P. Gentle, T. McJunkin, P.J. Hill, K.S. Myers, A.W. Abboud, R. Renwick, D. Hengst, Improvement of transmission line ampacity utilization by weather-based dynamic line rating, IEEE Trans. Power Deliv. 33 (4) (2018) 1853–1863.
[10] U.S. Department of Energy, Dynamic line rating report to congress, Tech. Rep., U.S. Department of Energy, Office of Electricity, 2019, [Online]. Available: https://www.energy.gov/oe/articles/dynamic-line-rating-report-congress-june-2019. (Accessed 30 January 2025).
[11] N.H. Abas, M.Z.A. Ab Kadir, N. Azis, J. Jasni, N.F. Ab Aziz, Z.M. Khurshid, Optimizing grid with dynamic line rating of conductors: a comprehensive review, IEEE Access 12 (2024) 9738–9756.
[12] E. Fernandez, I. Albizu, M.T. Bedialauneta, A.J. Mazon, P.T. Leite, Review of dynamic line rating systems for wind power integration, Renew. Sustain. Energy Rev. 53 (2016) 80–92.
[13] I. Daminov, A. Blavette, S. Bourguet, H.B. Ahmed, T. Soulard, P. Warlop, Economic performance of an overplanted offshore wind farm under several commitment strategies and dynamic thermal ratings of submarine export cable, Appl. Energy 346 (2023) 121326.
[14] T.V.M. Nielsen, S. Jakobsen, M. Savaghebi, Dynamic rating of three-core XLPE submarine cables for offshore wind farms, Appl. Sci. 9 (4) (2019) 800.
[15] S.L.R. Consulting, Dynamic thermal ratings for subsea cable systems, 2024, Accessed Jan. 29, 2025. [Online]. Available: https://www.slrconsulting.com/us/insights/dynamic-thermal-ratings-for-subsea-cable-systems/.
[16] R. Olsen, J. Holboell, U.S. Gudmundsdottir, Electrothermal coordination in cable based transmission grids, IEEE Trans. Power Syst. 28 (4) (2013) 4867–4874.

[17] D. Chatzipetros, J.A. Pilgrim, Review of the accuracy of single core equivalent thermal model for offshore wind farm cables, IEEE Trans. Power Deliv. 33 (4) (2017) 1913–1921.
[18] S.H.H. Kazmi, B. Cordes, J. Holbøll, T.H. Olesen, T.S. Sørensen, Machine learning based temperature forecast for offshore windfarm export cables, in: CIGRE Session 2020, CIGRE (International Council on Large Electric Systems), 2020.
[19] A. Madariaga, J.L. Martı, I. Zamora, S. Ceballos, O. Anaya-Lara, et al., Effective assessment of electric power losses in three-core XLPE cables, IEEE Trans. Power Syst. 28 (4) (2013) 4488–4495.
[20] CIGRE Work Group B1.45, Thermal monitoring of cable circuits and grid operators use of dynamic rating systems, Tech. Rep., CIGRE Technical Brochure, 2019.
[21] M. Erdmann, J. Pilgrim, E. al., Towards active cable reburial monitoring using distributed Fiber-Optic sensing over 40km of a high voltage marine interconnector, in: Proceedings of Jicable: 10th International Conference on Insulated Power Cables, IEEE, Versailles, France, 2019.
[22] X. He, J. Teh, B. Alharbi, Reliability impact of dynamic thermal rating on power system under high wind penetration and frequency security constraints, Appl. Energy 400 (2025) 126536.
[23] C.-M. Lai, J. Teh, Network topology optimisation based on dynamic thermal rating and battery storage systems for improved wind penetration and reliability, Appl. Energy 305 (2022) 117837.
[24] T. Song, J. Teh, Coordinated integration of wind energy in microgrids: a dual strategy approach leveraging dynamic thermal line rating and electric vehicle scheduling, Sustain. Energy Grids Netw. 38 (2024) 101299.
[25] J.C. Butcher, Numerical Methods for Ordinary Differential Equations, third ed, John Wiley & Sons, 2016.
[26] J.-B. Hiriart-Urruty, C. Lemaréchal, Convex analysis and minimization algorithms i: fundamentals, Springer (1993) 10–15.
[27] S.H.H. Kazmi, J. Holbøll, T.H. Olesen, T.S. Sørensen, Thermoelectric modelling and optimization of offshore windfarm export systems-state of the art, in: 2019 1st Global Power, Energy and Communication Conference (GPECOM), IEEE, 2019, pp. 331–336.
[28] International Electrotechnical Commission, IEC 60853-2:1989/AMD1:2008 calculation of the cyclic and emergency current rating of cables. Part 2: cyclic rating of cables greater than 18/30 (36) kV and emergency ratings for cables of all voltages, International Electrotechnical Commission, Geneva, Switzerland, 2008, IEC 60853-2:1989/AMD1:2008.
[29] G.J. Anders, Rating of Electric Power Cables: Ampacity Computations for Transmission, Distribution, and Industrial Applications, IEEE Press, New York, NY, USA, 1997.
[30] A. Matine, C.-H. Bonnard, A. Blavette, S. Bourguet, F. Rongère, T. Kovaltchouk, E. Schaeffer, Optimal sizing of submarine cables from an electro-thermal perspective, in: European Wave and Tidal Conference (EWTEC), 2017.
[31] M. Diaz-Aguiló, F. De Leon, Introducing mutual heating effects in the ladder-type soil model for the dynamic thermal rating of underground cables, IEEE Trans. Power Deliv. 30 (4) (2015) 1958–1964.
[32] Cableizer, Loss factor shield, circulating currents, 2023 https://www.cableizer.com/documentation/lambda_11/ (Accessed 12 April 2025).
[33] Cableizer (online), Loss factor armour, 2023 https://www.cableizer.com/documentation/lambda_2/ (Accessed 12 April 2025).
[34] K.F. Goddard, J.A. Pilgrim, R. Chippendale, P.L. Lewin, Induced losses in three-core SL-type high-voltage cables, IEEE Trans. Power Deliv. 30 (3) (2014) 1505–1513.
[35] S.M. Noufal, G.J. Anders, Sheath losses correction factor for cross-bonded cable systems with unknown minor section lengths: analytical expressions, IET Gener. Transm. Distrib. 15 (5) (2021) 849–859.
[36] TenneT, Hollandse kust (West), 2024,. [Online]. Available: https://www.tennet.eu/nl/projecten/provincies/noord-holland/hollandse-kust-west (Accessed 24 March 2025) (Accessed 24 March 2025).: https://www.tennet.eu/nl/projecten/provincies/noord-holland/hollandse-kust-west (Accessed 24 March 2025) (Accessed 24 March 2025).
[37] IRO – The Association of Dutch Suppliers in the Offshore Energy Industry, Solarduck contract largest offshore floating solar plant at HKW offshore wind farm (RWE), 2024,. [Online]. Available: https://iro.nl/nl/nieuws-en-pers/solarduck-contract-largest-offshore-floating-solar-plant-at-hkw-offshore-wind-farm-rwe/ (Accessed 28 March 2025).
[38] ABB, XLPE submarine cable systems: attachment to XLPE land cable systems, 2010,. [Online]. Available: https://new.abb.com/docs/default-source/ewea-doc/xlpe-submarine-cable-systems-2gm5007.pdf (Accessed 5 January 2025).
[39] Energy Charts, Wind and solar energy profile and electricity market prices for the Netherlands, 2023,. [Online]. Available: https://energy-charts.info/index.html?l=en&c=NL (Accessed 12 March 2025).
[40] K. R. N. M. Institute, KNMI, the Dutch national weather service, 2024,. [Online]. Available: https://www.knmi.nl/nederland-nu/klimatologie/uurgegevens (Accessed 12 March 2025).
[41] COMSOL multiphysics® v. 6.3, 2023, COMSOL AB, Stockholm, Sweden: [Online]. Available https://www.comsol.com (Accessed August 2025).
[42] A.G. Gonzalez-Rodriguez, Review of offshore wind farm cost components, Energy Sustain. Dev. 37 (2017) 10–19, https://doi.org/10.1016/j.esd.2016.12.001